Boundary Layer Control of Buoyant Coastal Currents and the Establishment of a Shelfbreak Front*

DAVID C. CHAPMAN

Woods Hole Oceanographic Institution, Woods Hole, Massachusetts

(Manuscript received 30 August 1999, in final form 25 January 2000)

ABSTRACT

The bottom boundary layer exerts a powerful control over buoyant coastal currents that contact the bottom, providing a mechanism for trapping density fronts along isobaths. Recent observations suggest that this mechanism may play a role in shelfbreak front dynamics. Here previous studies are extended to investigate frontal trapping by the bottom boundary layer in deeper water typical of shelf breaks and in the presence of ambient stratification. A primitive-equation numerical model is used to study a buoyant current traveling along a vertical wall as it encounters shallow bottom topography typical of a continental shelf. At the initial point of contact, a surface-to-bottom front forms with an associated surface-intensified, geostrophic current. In the absence of bottom friction, the current shoals and continues along the shelf close to the coast. In the presence of bottom friction, buoyancy advection in the bottom boundary layer moves the front offshore (across isobaths) until it reaches a depth where the cross-isobath transport in the boundary layer nearly vanishes. The front remains trapped at this isobath, h_*, which can be estimated theoretically as a solution of

$$\frac{2N^2}{3\epsilon g}h_*^3 + h_*^2 - \frac{2T_0 f}{\epsilon g} = 0,$$

where T_0 is the transport in the inflowing buoyant current, ϵ is the density anomaly of the inflowing buoyant current divided by a reference density, N is the buoyancy frequency of the ambient water, f is the Coriolis parameter, and g is gravitational acceleration. With no ambient stratification ($N = 0$), h_* is identical to a previous estimate of the frontal trapping depth and agrees with the numerical calculations. Ambient stratification tends to maintain the front in shallower water, but not always as shallow as h_* because ambient water may join the frontal current, thereby increasing the frontal transport well beyond T_0. Nevertheless, h_* appears to provide bounds for the location of the trapped front.

The frontal trapping mechanism is remarkably robust, in fact so robust that the presence of a shelf break has little effect on the final location of the front. Bottom stress is necessary for the frontal trapping mechanism, but the trapping isobath is relatively insensitive to the magnitude of the bottom friction coefficient. The near-surface part of the front is sometimes unstable, but it can be stabilized either by ambient stratification or by a weak background current in the direction of the buoyant inflow.

1. Introduction

On some broad continental shelves, the accumulated influence of freshwater discharges dominates the large-scale circulation, establishing a fairly sharp change in water properties at or near the shelf break, typically separating relatively fresh and cold shelf waters from saltier and warmer slope waters. Such a shelfbreak front and its associated baroclinic currents are dominant features of the coastal circulation, strongly influencing both the alongshelf and cross-shelf transports of mass, momentum, nutrients, sediments, etc.

The best known (and most studied) example is the coastal circulation along the east coast of North America from the northern Labrador shelf to Cape Hatteras [e.g., see Loder et al. (1998) and the references therein]. Oxygen isotope measurements show that much of the continental shelf water found in the Middle Atlantic Bight (MAB) from Georges Bank to Cape Hatteras has a northern origin, at least as far north as the northern Labrador shelf (e.g., Chapman and Beardsley 1989; Khatiwala et al. 1999), suggesting some continuity of generally southward transport over this distance. The details of the transit, however, are largely uncertain. There is considerable loss of shelf water along the way, but precisely where and by what processes remains unclear. Nevertheless, a persistent shelfbreak front is present along much of the Labrador shelf and through the

* Woods Hole Oceanographic Institution Contribution Number 10033.

Corresponding author address: David C. Chapman, Woods Hole Oceanographic Institution, Woods Hole, MA 02543.
E-mail: dchapman@whoi.edu.

MAB. It is particularly intriguing that the front remains close to the shelf break despite the fact that the shelf break is located at about 200-m depth along the Labrador shelf, whereas it occurs at about 100 m in the MAB. How the front and flow adjust and how/if the loss of transport is related to changes in the topography are unknown.

The shelfbreak front in the MAB has been studied for many years, long enough to produce a climatology (Linder and Gawarkiewicz 1998), and it is known to be quite variable. Recent observations at high resolution in both space and time have revealed even more complexity than previously anticipated (Pickart et al. 1999; Gawarkiewicz et al. 1999, submitted to *J. Phys. Oceanogr.*). Small-scale (5–10 km) hydrographic features and narrow baroclinic jets appear within the frontal region and then change or disappear within a few days. External forcing (e.g., offshore eddies) can produce large changes in the frontal position, flow direction, and property gradients. Yet, the shelfbreak front is robust and resilient on long timescales; that is, it is virtually always present in some form, suggesting that some basic dynamics must be at work to establish and maintain the front despite such complications. If so, idealized process modeling should be capable of revealing these underlying dynamics.

There have been two basic approaches to modeling the steady or long-timescale behavior of a shelfbreak front. One approach considers the gradual filling of a two-dimensional (cross-shelf and vertical) frictionless shelf with freshened water from a local source (e.g., Condie 1993; Willmott and Collings 1997), an idea that can be traced back to Stommel and Leetma (1972), who considered a flat-bottom shelf. As the front separating fresher and ambient waters reaches the shelf edge, potential vorticity conservation restricts the continued seaward motion, thereby establishing the front at the shelf break. However, these models neither address the alongshelf formation and maintenance of the front nor account for the remote origin of the shelf water (northern source for the MAB) because the models are two-dimensional and the fresher water is supplied locally. Furthermore, the behavior depends critically on potential vorticity conservation, which is unlikely over the shelf where bottom friction typically generates a boundary layer that occupies an appreciable portion of the water column.

The second approach considers the three-dimensional evolution of an alongshelf current and the critical role of the bottom boundary layer. Wright (1989) showed that offshore Ekman transport in the bottom boundary layer, caused by an imposed alongshelf current, can carry an existing surface-to-bottom front to the edge of a step shelf. Continued Ekman transport drains the alongshelf flow from the shelf, causing the foot (or base) of the front to move gradually downward along the face of the step until it reaches an equilibrium position where it carries all of the alongshelf flow. Gawarkiewicz and Chapman (1992) examined the adjustment of a barotropic flow in an initially uniformly stratified coastal ocean and suggested that the action of the bottom boundary layer could itself form a front at the shelf break, where convergence within the bottom boundary layer causes flow to leave the bottom, moving upward along isopycnals.[1] Chapman and Lentz (1994) examined the alongshelf evolution of a surface-to-bottom front formed by a local freshwater discharge over a uniformly sloping shelf. This, in some respects, is a combination of the Wright (1989) and Gawarkiewicz and Chapman (1992) models. The front moves offshore under the influence of bottom Ekman transport similar to Wright's model, but over a sloping bottom with nonlinear advection of density in the bottom boundary layer playing a leading role. Eventually the depth becomes great enough that the alongshelf current (and hence Ekman transport) changes sign at the bottom. This creates a strong convergence in the bottom boundary layer that causes flow to leave the bottom and move upward along the front, as in the Gawarkiewicz and Chapman model. The front is then trapped at this isobath and does not move farther offshore (except perhaps due to small viscous and diffusive effects). Yankovsky and Chapman (1997) later derived a simple approximation for the trapping isobath

$$h_b = (2T_0 f/\epsilon g)^{1/2}, \tag{1}$$

where T_0 is the transport of the buoyant inflow (assumed to be entirely carried within the front), f is the Coriolis parameter, g is gravitational acceleration, and $\epsilon = \Delta\rho/\rho_0$ with $\Delta\rho$ being the density anomaly of the buoyant source and ρ_0 the ambient density. Presumably, if h_b is close to the shelfbreak depth, then the front would stop there and be a shelfbreak front. However, this was not demonstrated by either Chapman and Lentz (1994) or Yankovsky and Chapman (1997) because an enormous alongshelf distance is required for the front created by the freshwater discharge to reach the shelf break across a wide shelf like the MAB. Other processes, such as diffusion, may substantially alter the front over this distance (e.g., Garvine 1999; Narayanan 1999).

Some recent observations suggest that the frontal trapping mechanism just described may play a role in shelfbreak front dynamics. In a remarkable set of experiments, Houghton (1997) and Houghton and Visbeck (1998) released dye tracer near the foot of the MAB shelfbreak front, which clearly demonstrated convergent flow in the bottom boundary layer that leaves the bottom there and flows upward along frontal isopycnals. Further support for this flow structure has since been reported

[1] The recent study by Chapman and Lentz (1997) shows that this flow is unlikely to form a surface-to-bottom front at shelfbreak depths if vertical mixing is primarily confined to the bottom boundary layer. However, boundary layer separation from the bottom remains a robust feature of the model.

in observations of chlorophyll and suspended material (Barth et al. 1998) as well as hydrography and shipboard velocity measurements (Pickart 2000). Encouraged by these results, an attempt is made here to build on the previous modeling efforts to address several outstanding issues. For example, how can a front be established at typical shelfbreak depths within a reasonable alongshelf distance? How well does the relation (1) work at such depths? Is the trapping isobath sensitive to the strength of bottom friction? How does ambient stratification alter (1)? Finally, can this model explain the location of the front at the shelf break (i.e., what is special about the shelf break)?

To address these issues, a primitive equation numerical model is used in fairly idealized settings, as described in section 2. The powerful control that the bottom boundary layer exerts on the front is demonstrated in section 3. The effects of ambient stratification on the trapping of a buoyant inflow are investigated in section 4. The influence of shelfbreak topography is examined in section 5, followed by a discussion in section 6 and a summary in section 7.

2. Numerical model

a. Equations

A variety of model domains, topographies, and stratifications are used in the following calculations. In each case the *s* coordinate primitive equation model (SPEM5.1), developed by D. Haidvogel's group at Rutgers University, is used to solve the following hydrostatic and Boussinesq momentum, density, and continuity equations:

$$u_t + \mathbf{u}\cdot\nabla u - fv = -\frac{1}{\rho_0}p_x + (A_V u_z)_z + F_u \quad (2)$$

$$v_t + \mathbf{u}\cdot\nabla v + fu = -\frac{1}{\rho_0}p_y + (A_V v_z)_z + F_v \quad (3)$$

$$p_z = -\rho g \quad (4)$$

$$\rho_t + \mathbf{u}\cdot\nabla\rho = (K_V\rho_z)_z + F_\rho \quad (5)$$

$$\nabla\cdot\mathbf{u} = 0. \quad (6)$$

In this system (u, v, w) represent the (x, y, z) components of the velocity $\mathbf{u}$ with z directed vertically upward from the ocean surface, ρ is the difference between the total density and a constant reference density ρ_0, p is pressure, f is the Coriolis parameter, g is gravitational acceleration, A_V is the vertical eddy viscosity, K_V is the vertical eddy diffusivity, and t is time. Variables $F_{u,v,\rho}$ represent dissipative functions that are required for numerical stability. Subscripts x, y, z, and t denote partial differentiation.

SPEM5.1 is similar to earlier versions of SPEM (e.g., Haidvogel et al. 1991). The most important differences are that SPEM5.1 approximates the system (2)–(6) with finite differences in both horizontal and vertical directions, and a generalized stretched vertical coordinate [the s coordinate described by Song and Haidvogel (1994)] allows greater flexibility in specifying the locations of vertical grid points. For the present calculations, the grid points are concentrated near the bottom, in order to resolve the bottom boundary layer, by using the following s-coordinate mapping

$$z(s) = h_c s + (h - h_c)\{\sinh[\theta(s+1)]/\sinh\theta - 1\}, \quad -1 \le s \le 0, \quad (7)$$

where $h(x, y)$ is the bottom depth, while h_c is the shallowest depth and θ is a prescribed constant.

There are no fluxes of density or momentum at the surface or any solid boundaries. At the bottom, the density flux is zero, while the shear stress is specified using a linear bottom stress parameterization,

$$A_V u_z = ru; \qquad A_V v_z = rv \quad \text{at } z = -h, \quad (8)$$

where r is a bottom friction coefficient.

The vertical mixing coefficients A_V and K_V are approximated using the Mellor–Yamada level 2 turbulence closure scheme as applied in SPEM5.1. This is a slightly simplified version of the standard scheme in that the maximum mixing length scale is assumed independent of z to avoid the need for iterations. Also, a maximum value of 10^{-3} m^2 s^{-1} is imposed to reduce numerical errors in the finite difference approximations of the vertical mixing terms. The minimum value for A_V and K_V is 10^{-5} m^2 s^{-1}. Additional vertical mixing of density is applied in the form of instantaneous convective adjustment whenever the water column becomes statically unstable (i.e., when lighter water appears under heavier water). In the present calculations, this occurs only within the bottom boundary layer.

For numerical stability, Laplacian subgridscale mixing with constant mixing coefficients is applied along horizontal surfaces (i.e., $F_{u,v,\rho} = \nu_{u,v,\rho}\nabla^2 u, v, \rho$), using the smallest mixing coefficients that produce stable calculations; $\nu_{u,v} = 20$ m^2 s^{-1} and $\nu_\rho = 5$ m^2 s^{-1}.

b. Configuration

The model configuration is designed to test the idea that local bathymetry may be responsible for establishing a trapped front at shelfbreak depths within a relatively short alongshelf distance. For example, along the northern Labrador shelf (Fig. 1a), the buoyant Baffin Current must negotiate Hudson Strait (61°N) before moving onto the Labrador shelf. North of the strait, the current flows along very steep topography, with a front at about 200-m depth (e.g., Lazier and Wright 1993, their Fig. 15). South of the strait, the shelf (indicated by the 200-m isobath) widens rather abruptly, and the front is attached close to the shelf break, still at about 200 m. Similarly, most of the buoyant water entering the MAB shelf flows around the northern flank and tip

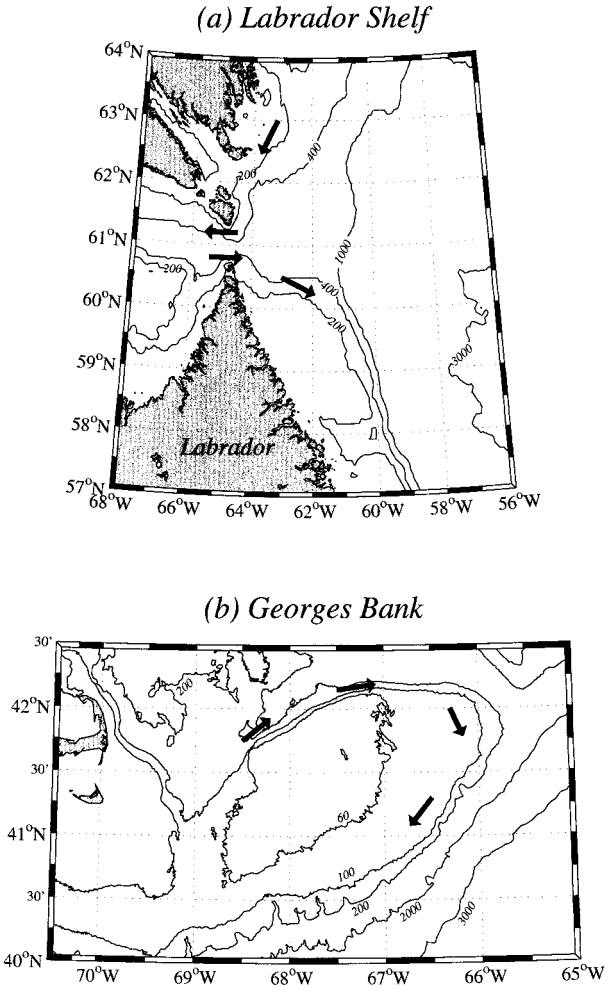

FIG. 1. Bathymetry on (a) the northern Labrador shelf and (b) Georges Bank. Arrows indicate basic flow direction (but not magnitude) of mean flows.

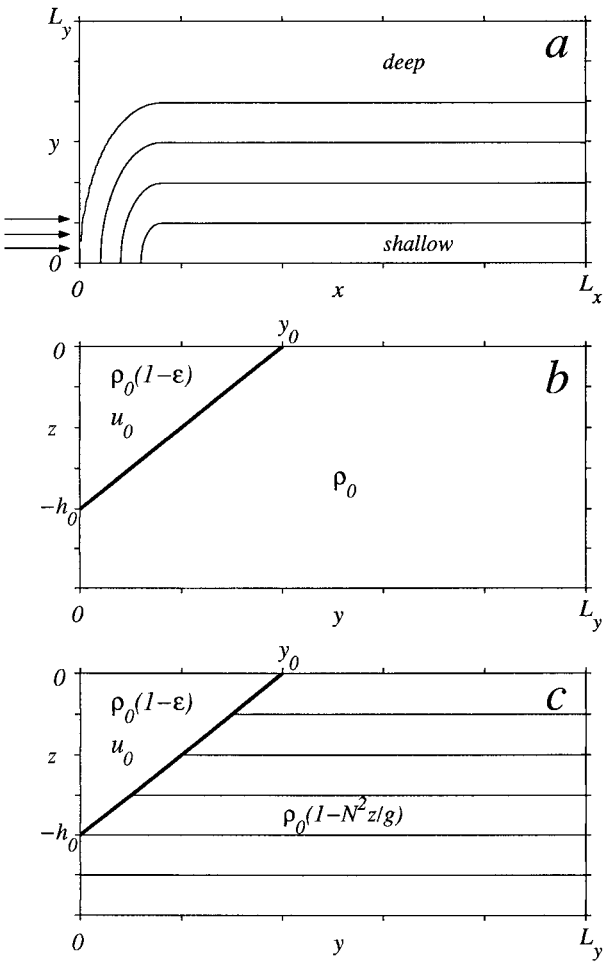

FIG. 2. Model domain and inflow conditions (looking upstream). (a) Plan view showing typical bottom topography with shallower water along $y = 0$. Arrows indicate location of buoyant inflow. (b) Inflow condition with a homogeneous ambient fluid. (c) Inflow condition with ambient stratification.

of Georges Bank, where the bottom slope is unusually steep, before encountering the gentler slopes of the southern flank of the bank (Fig. 1b). The shelfbreak front is established almost immediately on the southern flank of the bank and is sharpest there in all seasons (Ullman and Cornillon 1999). In both locations, a buoyant coastal current flows along bathymetry that changes abruptly from a very steep bottom slope to a gentle bottom slope typical of a continental shelf.

The model domain, bottom topography, and inflow conditions are chosen to capture the essence of this scenario (Fig. 2). The model domain is a uniformly rotating ($f = 10^{-4}$ s^{-1}) straight channel with solid walls at the coast ($y = 0$) and offshore ($y = L_y$) and open boundaries at $x = 0$ and $x = L_x$ (Fig. 2a). The bottom is flat at the upstream end ($x = 0$), rises rapidly in the x direction, and becomes invariant in x for the remainder of the channel; that is, the isobaths become parallel to the coast. The bottom topography in the uniform region consists of either a single slope or two slopes with a shelf break, always with a coastal depth of $h_c = 50$ m ($y = 0$). Each calculation begins from rest. A buoyant geostrophic inflow with velocity u_0 and density $\rho_0(1 - \epsilon)$ is prescribed at $t = 0$ in a triangular region at the upstream boundary ($x = 0$) with depth h_0 and extending offshore a distance y_0 (Figs. 2b,c). The remainder of the fluid is at rest with either constant density ρ_0 (Fig. 2b) or stable stratification characterized by a constant buoyancy frequency $N = (-g\rho_z/\rho_0)^{1/2}$ with density ρ_0 at the surface (Fig. 2c). All variables on this inflow boundary remain fixed at their intial values throughout the calculation. Thus, each of the questions posed in the introduction can be addressed with this idealized model configuration.

A radiation condition is applied at the downstream boundary ($x = L_x$) as follows. The interior barotropic vorticity is advected to the boundary and used to compute the barotropic streamfunction there (after assuming that the curvature of the stream function in x vanishes).

Then the interior density and depth-varying velocities are advected to the boundary. This condition produces better results than a wavelike radiation condition and/or a sponge, presumably because of the advective nature of the interior flows. The most significant effect of this imperfect open boundary condition occurs with ambient stratification when baroclinic Kelvin waves (primarily first-mode) are generated at the open boundary and move along the deep boundary in the $-x$ direction toward the inflow boundary where they continue around the corner and affect the inflow. These spurious Kelvin waves are effectively eliminated by lengthening and widening the channel while applying a Rayleigh-damping sponge along the entire deep boundary.

For calculations with constant ambient density, the domain size is $L_x = 150$ km and $L_y = 80$ km with uniform grid spacing of 1.6 km in each direction. For calculations with ambient stratification, the domain is larger ($L_x = 250$ km, $L_y = 120$ or 200 km). Increased length is efficiently achieved by stretching the grid with $\Delta x = 1.6$ km for $x < 125$ km and gradually increasing to $\Delta x = 4.3$ km at $x = L_x$. Grid stretching in y allows space for the offshore sponge layer. When $L_y = 120$ km, $\Delta y = 1.6$ km for $y < 80$ km and gradually increases to $\Delta y = 4.7$ km at $y = L_y$; the sponge layer is 35 km wide. When $L_y = 200$ km, $\Delta y = 2.7$ km for $y < 132$ km and gradually increases to $\Delta y = 7.9$ km at $y = L_y$; the sponge layer is 60 km wide. Only results from the high resolution parts of the model domain are shown here, and they appear to be insensitive to the grid differences, provided that the Kelvin waves are eliminated.

Vertical resolution varies with depth according to (7) with 30 grid points. At the shallowest depth ($h = h_c$ at $y = 0$) the grid spacing is uniform with $\Delta z = 1.72$ m. The choice of $\theta = 2.5$ in (7) yields smaller grid spacing near the bottom at all depths such that, where $h = 250$ m (the deepest depth used in any calculation), $\Delta z = 4.4$ m at the bottom and $\Delta z = 17$ m at the surface. The flows considered here do not reach depths much below about 150 m, so they are reasonably well resolved throughout.

Each calculation continues until the isopycnals at the bottom have essentially reached a steady state everywhere in the channel. This typically requires between 100 and 200 days of simulation time, varying somewhat with model parameters. The time step is 432 seconds.

3. Boundary layer control

The accuracy of (1) in predicting the frontal trapping isobath at depths typical of shelf breaks is tested here using the inflow shown in Fig. 2b for a range of parameters. There is no ambient stratification in these calculations. The buoyant inflow is assumed geostrophic, which places constraints on the inflow parameters. For a two-layer geostrophic flow with a motionless lower layer, the velocity along the front is proportional to the slope of the interface; $u = -\epsilon g \zeta_y / f$ where ζ is the thickness of the upper layer. Assuming the inflow to be of this form, the inflow transport is

$$T_0 = \int_0^{y_0} u\zeta \, dy = \epsilon g h_0^2 / 2f, \tag{9}$$

where $\zeta = 0$ at $y = y_0$ has been used. Rearranging, (9) becomes

$$h_0 = (2T_0 f / \epsilon g)^{1/2}. \tag{10}$$

Not surprisingly, h_0 is identical to the final frontal depth found by Wright (1989) with T_0 representing his imposed alongshelf transport, because at that point Wright's flow is a two-layer geostrophic flow along a vertical wall. Two features of (10) are noteworthy. First, h_0 is independent of the shape of the interface, depending only on the transport, the density anomaly, and f. Second, and more importantly, h_0 is identical to h_b in (1). This means that, if the density difference across the downstream front is the same as at the inflow and if the entire inflow transport is carried within the downstream front, then the frontal trapping depth will be identical to the depth of the inflow at the coast.

At first glance, this result may seem intuitive because a geostrophic flow should follow isobaths (on an f plane) to conserve potential vorticity. However, this is strictly true only for perfectly geostrophic flows. Any ageostrophic effects allow flows to cross isobaths. For example, nonlinear momentum advection can produce large relative vorticities, causing flows to cross isobaths (e.g., flow over seamounts) while still conserving potential vorticity. Several examples are presented below. Furthermore, potential vorticity is not conserved where bottom friction is present. In fact, bottom stress breaks the geostrophic constraint to follow isobaths by changing the potential vorticity, and this is the crux of the mechanism that moves the front offshore (across isobaths) and ultimately traps it. Indeed, in cases of frontal trapping by the bottom boundary layer, it seems paradoxical that bottom stress should change the potential vorticity, yet move the front to the same location it would have if the flow were perfectly geostrophic and potential vorticity were conserved. In a sense, bottom stress defeats itself.

A number of calculations have been made to test these ideas. In each case, the inflow shape is shown in Fig. 2b. The inflow transport T_0 and relative density anomaly ϵ are chosen so that the inflow depth h_0 coincides with an isobath that is near the center of the model domain in the downstream region of uniform topography. Then y_0 is chosen small enough that the front must move offshore to follow the h_0 isobath. Finally, the inflow velocity u_0 must satisfy $T_0 = u_0 h_0 y_0 / 2$. Note that the actual transport introduced in the model is not exactly T_0 because of the finite size of the grid elements in the numerical model. Therefore, in what follows, T_0 is taken to be the actual model transport rather than the product

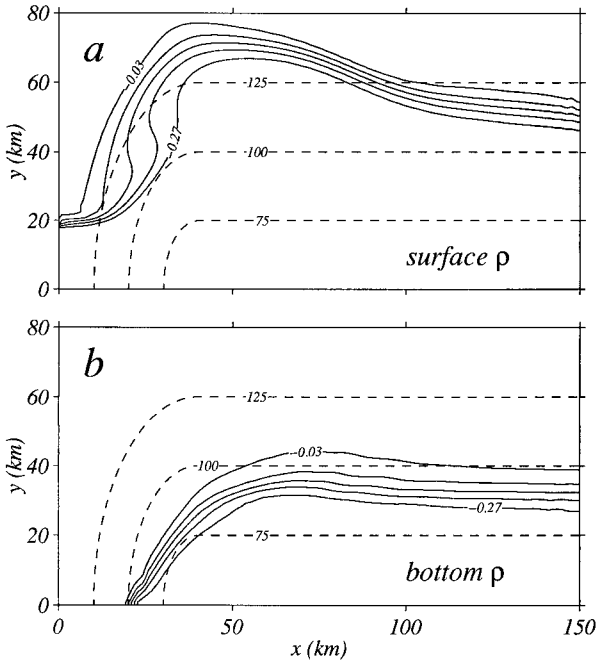

FIG. 3. Plan views of (a) surface and (b) bottom density anomalies after $t = 150$ days of a buoyant inflow into a homogeneous fluid. Parameters are $\epsilon = 3 \times 10^{-4}$, $T_0 = 0.1365 \times 10^6$ m^3 s^{-1}, $h_0 = 100$ m, $y_0 = 20$ km, $f = 10^{-4}$ s^{-1}, and $r = 5 \times 10^{-4}$ m s^{-1}. Contour interval is 0.06 kg m^{-3}. Dashed curves are selected isobaths.

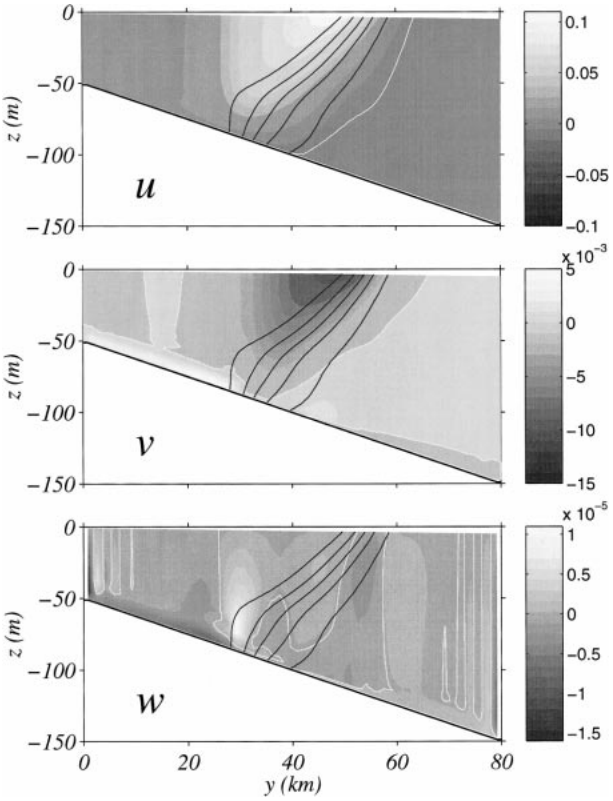

FIG. 4. Vertical sections of velocity and density anomaly for the calculation shown in Fig. 3 at $x = 120$ km. Velocity values (m s^{-1}) are given by the shading bar at right. White contours mark zero velocities. Density anomaly contours are -0.27 to -0.03 by 0.06 kg m^{-3} with the lightest water closest to $y = 0$.

of the inflow parameters. The difference is typically only about 5%.

All of the calculations produce qualitatively similar results, a typical example of which is shown in Figs. 3 and 4. Parameters are $h_0 = 100$ m, $y_0 = 20$ km, $u_0 = 0.147$ m s^{-1}, $\epsilon = 3 \times 10^{-4}$, and $r = 5 \times 10^{-4}$ m s^{-1}. Plan views of the surface and bottom density anomalies after 150 days show that the inflow first contacts the bottom topography near the 100-m isobath as expected (Fig. 3b). The foot of the front does not follow this isobath closely in the turning region ($x < 40$ km), but it is reestablished near the 100-m isobath by about $x = 60$ km (i.e., $h_b \approx h_0$). This bottom density anomaly pattern remains fixed in time, but the surface expression of the front does not (Fig. 3a). Instead, a smooth bulge forms and slowly grows toward the offshore boundary, much like the bulge formed by a surface-trapped freshwater inflow from a coastal source (e.g., Fong 1998). One effect of the growing bulge is to slightly reduce the transport available for the downstream front, so the front is trapped at a shallower isobath than given by (1).

The velocity and density structures of the trapped front (Fig. 4) are qualitatively similar to those found by Chapman and Lentz (1994). The alongshelf velocity is concentrated in a narrow surface-intensified jet over the front. A sharp convergence in the cross-shelf velocity at the foot of the front coincides with a strong upward vertical velocity on the shoreward side of the front. There are also some interesting differences. For example, the front in Fig. 4 narrows toward the surface, allowing greater surface intensification of the alongshelf current. Neither the alongshelf nor the cross-shelf current changes sign beneath the front, and the vertical velocity shows little indication of the counterrotating cells that extend throughout the water column in the Chapman and Lentz (1994) model. These differences are all attributable to differences in the treatment of vertical mixing. Chapman and Lentz (1994) used constant mixing coefficients equal to the maximum values used here. This restricts the frontal structure throughout the water column, leading to nearly uniform vertical shear, considerably stronger cross-shelf velocities near the surface and, hence, the counterrotating cells. Variable mixing coefficients allow greater variations in Ekman layer thickness and, therefore, more flexibility in frontal adjustment (e.g., note the horizontal variations in isopycnal slope near the bottom).

A variety of calculations like that in Figs. 3 and 4 were made to test the sensitivity to various parameters. First, calculations were made with $y_0 = 10$ and 30 km, while adjusting u_0 to give the same transport and keeping all other parameters the same. The primary change is that the alongshelf distance over which the front reaches the trapping isobath is longer for larger u_0 be-

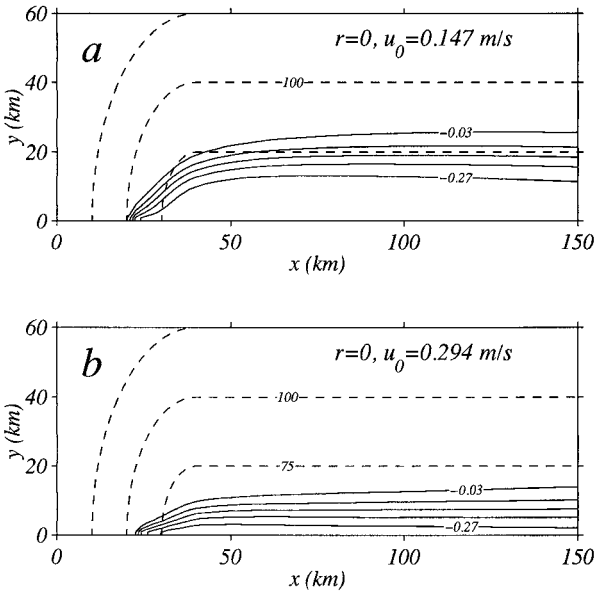

FIG. 5. Plan views of bottom density anomalies after $t = 100$ days of a buoyant inflow into a homogeneous fluid with no bottom stress ($r = 0$). Both cases have the same transport as Fig. 3 but (a) has the same inflow velocity while (b) has twice the inflow velocity. Other parameters are $\epsilon = 3 \times 10^{-4}$, $T_0 = 0.1365 \times 10^6$ m^3 s^{-1}, $h_0 = 100$ m, $f = 10^{-4}$ s^{-1}. Contour interval is 0.06 kg m^{-3}. Dashed curves are selected isobaths. Only part of each model domain is shown; $L_y = 80$ km.

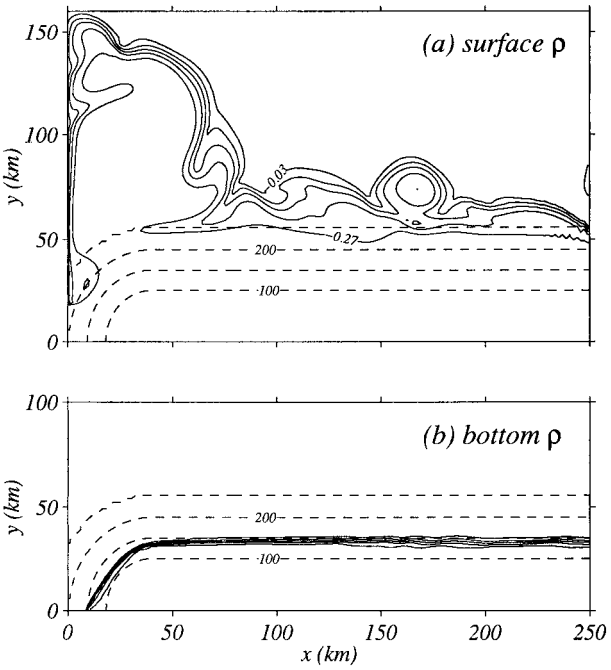

FIG. 6. Plan views of (a) surface and (b) bottom density anomalies after $t = 210$ days of a buoyant inflow into a homogeneous fluid. Parameters are $\epsilon = 3 \times 10^{-4}$, $T_0 = 0.3052 \times 10^6$ m^3 s^{-1}, $h_0 = 150$ m, $y_0 = 20$ km, $f = 10^{-4}$ s^{-1}, $r = 5 \times 10^{-4}$ m s^{-1}. Contour interval is 0.06 kg m^{-3}. Dashed curves are selected isobaths.

cause of increased momentum advection. However, the trapping isobath is virtually unchanged. Next, the strength of bottom friction was varied with $r = 1$, 10, and 20 ($\times 10^{-4}$ m s^{-1}). The resulting changes are minor; with larger r, the front moves to a slightly deeper trapping isobath in a slightly shorter alongshelf distance. For very weak bottom friction ($r = 2 \times 10^{-5}$ m s^{-1}) the front moves offshore very slowly and does not reach the trapping depth within the model domain. The flow then resembles the frictionless cases described below. Several calculations were made with increased ϵ and T_0 such that h_0 remained at 100 m, with almost no change in frontal trapping. Finally, calculations were made with $h_0 = 75$ and 150 m, and in every case the front becomes trapped near the h_0 isobath, consistent with (1).

To demonstrate the fundamental importance of bottom stress in trapping the front, three calculations were made with no bottom friction ($r = 0$). Each calculation has $h_0 = 100$ m as in Figs. 3 and 4, but different combinations of u_0 and y_0. Whereas the frontal trapping position is essentially unaltered by the *magnitude* of bottom stress, its *presence* is of great importance (Fig. 5). Without bottom friction, the position of the foot of the front is primarily determined by the inflow velocity. Stronger inflow leads to greater influence of nonlinear momentum advection (i.e., higher Rossby number and increased relative vorticity), which causes the flow to cross isobaths more easily, as occurs with deep-ocean flows over seamounts, for example. A repeat of the calculation shown in Fig. 3, but without bottom friction, shows that the foot of the front is substantially closer to the coast (Fig. 5a), and the front stays even closer to the coast for larger u_0 (Fig. 5b). In these cases, the surface bulge (not shown) does not form. Thus, without bottom stress, the frontal trapping mechanism is absent, so the front is not moved to h_b.

The frontal trapping mechanism is incredibly robust and stable. For example, the near-surface portion of the front tends to be less stable in deeper water ($h_0 = 150$ m) than in shallower water ($h_0 = 75$ or 100 m). The surface bulge grows rapidly, and the front contains many small-scale oscillations and eddies that evolve quickly (Fig. 6a). Yet, the foot of the front exhibits virtually no motion and is locked onto an isobath (Fig. 6b). In fact, no signs of instabilities at the foot of the front appeared in any of the calculations.

A comparison of the trapping isobath found in the numerical calculations with the approximation (1) appears in Fig. 7. For each calculation the trapping isobath is defined as the depth at which the middle isopyncal ($\rho = -\epsilon/2$) intersects the bottom in the downstream region where the front is parallel to the isobaths, and is plotted against h_b from (1). Circles represent cases with bottom friction ($r \geq 10^{-4}$ m s^{-1}) and diamonds those without bottom friction ($r = 0$). The solid line represents perfect agreement between numerical model and theory. The agreement is good for most of the calculations with bottom friction. There is a tendency for the trapping

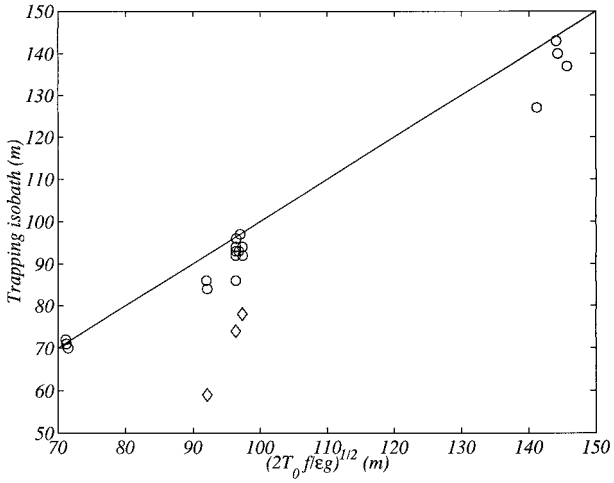

FIG. 7. Trapping isobath from the numerical calculations vs h_b given by (1). Circles are frictional cases ($r \geq 10^{-4}$ m s^{-1}); diamonds are frictionless cases ($r = 0$). The straight line indicates perfect agreement.

depth to be slightly less than the theoretical value, in part owing to the growing surface bulge described above. The discrepancy also tends to be greater for larger inflow velocities, suggesting the influence of nonlinear momentum advection. As expected, cases without bottom stress are farthest from the theoretical line, and the disagreement increases with increasing u_0. It appears that (1) is a good approximation for the trapping isobath, provided bottom friction is present.

4. Ambient stratification

In this section, the effects of ambient stratification (see Fig. 2c) on frontal trapping are explored. The motivation is twofold. First, the ocean is not homogeneous, so ambient stratification is a step toward realism. Second, adding ambient stratification provides a way of explicitly linking studies of a buoyant inflow into a homogeneous ocean (as in section 3) to those at the opposite extreme in which a nonbuoyant barotropic inflow enters a stratified ocean (e.g., Gawarkiewicz and Chapman 1992; Chapman and Lentz 1997). The former impose a front and follow its evolution under the influence of the bottom boundary layer. The latter suggest that bottom boundary layer dynamics alone can create fronts from the ambient stratification, without the need for an imposed buoyant inflow. Although the action of the bottom boundary layer is unlikely to create a surface-to-bottom front over the shelf (Chapman and Lentz 1997), it can generate regions of increased horizontal density gradients and convergence within the bottom boundary layer, which might substantially change the downstream trapping isobath found in section 3.

If the basic frontal trapping mechanism is not changed by ambient stratification, then a theoretical estimate of the new trapping isobath is possible. Suppose the buoyant inflow forms a narrow surface-to-bottom front as in section 3, but now with stratified offshore waters (as sketched in Fig. 8). Further assume that the alongshelf flow is in thermal wind balance ($u_z = g\rho_y/\rho_0 f$) and that the front is trapped in a region (between y_1 and y_2) where the alongshelf velocity vanishes at the bottom. With these assumptions, the frontal transport can be written (after integrating once by parts)

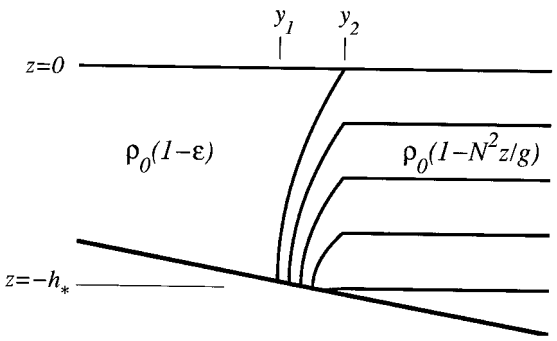

FIG. 8. Sketch of the idealized frontal configuration used to derive (14) for h_*, the trapping isobath with ambient stratification. The front is located between y_1 and y_2.

$$T_s = \int_{y_1}^{y_2}\int_{-h}^{0} u\, dz\, dy = -\frac{g}{\rho_0 f}\int_{y_1}^{y_2}\int_{-h}^{0} \rho_y z\, dz\, dy. \quad (11)$$

After applying Leibnitz' rule, (11) can be rewritten as

$$T_s = -\frac{g}{\rho_0 f}\left(\int_{-h}^{0} \rho z\, dz|_{y_2} - \int_{-h}^{0} \rho z\, dz|_{y_1}\right) - \frac{g}{\rho_0 f}\int_{y_1}^{y_2} h h_y \rho_b\, dy, \quad (12)$$

where ρ_b is the density at the bottom. The vertical integrals can be evaluated by assuming uniform stratification on the deep side of the front ($\rho/\rho_0 = 1 - N^2 z/g$ at $y = y_2$) and constant density on the shallow side ($\rho/\rho_0 = 1 - \epsilon$ at $y = y_1$). If the front is sufficiently narrow [$h(y_2) - h(y_1) \ll h_*$], then the last term in (12) is negligible and the depths at y_1 and y_2 are nearly equal to the new trapping depth h_*. The transport in the stratified front then becomes

$$T_s = \frac{N^2}{3f}h_*^3 + \frac{\epsilon g}{2f}h_*^2, \quad (13)$$

which is a cubic polynomial in h_* and can be rewritten

$$\frac{2N^2}{3\epsilon g}h_*^3 + h_*^2 - \frac{2T_s f}{\epsilon g} = 0. \quad (14)$$

The effect of ambient stratification appears in the cubic term. If stratification vanishes ($N = 0$), then (14) reduces to (1) with $h_* = h_b$ (assuming $T_s = T_0$). At the other extreme, if the inflow is not buoyant ($\epsilon = 0$), then the quadratic term in (14) vanishes and $h_* = (3T_s f/N^2)^{1/3}$. According to the Chapman and Lentz (1997) model, the depth that such a barotropic inflow

into a stratified fluid reaches in its downstream equilibrium scales as $h_{CL} \sim (F_0 f/N^2)^{1/2}$, where F_0 is the transport per unit depth. Written in terms of transport, this becomes $h_{CL} \sim (T_s f/h_{CL}N^2)^{1/2}$, which, when solved for h_{CL} yields $h_{CL} \sim (T_s f/N^2)^{1/3}$, in agreement with (14) when $\epsilon = 0$. Thus, (14) represents a dynamical link between a buoyant inflow into a homogeneous fluid and a barotropic inflow into a stratified fluid. Finally, writing $\hat{h}_* = h_*/(2T_0 f/\epsilon g)^{1/2}$ and setting $T_s = T_0$, (14) can be written

$$\gamma \hat{h}_*^3 + \hat{h}_*^2 - 1 = 0 \tag{15}$$

where

$$\gamma = \left(\frac{2N^2}{3\epsilon g}\right)\left(\frac{2T_0 f}{\epsilon g}\right)^{1/2}$$

in which the single dimensionless parameter γ determines the scaled trapping isobath.

Solutions of (15) obtained from a standard formula (e.g., Abramowitz and Stegun 1968) show that only one positive real solution exists for $\gamma \geq 0$, and this solution is a decreasing function of γ, starting from $\hat{h}_* = 1$ at $\gamma = 0$. Smaller $\hat{h}_*$ corresponds to a shallower trapping isobath. That is, ambient stratification traps the front closer to the coast. Physically, ambient stratification allows increased horizontal density gradients with depth and, therefore, larger vertical shears in the alongshelf current. Increased vertical shear reduces the alongshelf velocity at the bottom to zero in shallower water, thus trapping the front closer to the coast.

To test these ideas, numerical calculations have been made like those in section 3, except that the ambient fluid is uniformly stratified with buoyancy frequency N (Fig. 2c). The inflow is no longer precisely geostrophic, but the adjustment process is qualitatively unchanged by the presence of ambient stratification. The inflow moves up the topography, spreads some distance offshore, and adjusts to a nearly steady state in which the bottom isopycnals are almost parallel to the isobaths. Examples of the vertical structure of the alongshelf velocity and density anomaly in the downstream steady flow with different ambient stratifications are shown in Fig. 9. All other parameters are the same as the calculation shown in Figs. 3 and 4. The dashed density anomaly contours show buoyant inflow water, while the solid contours show ambient water. The effect of weak ambient stratification (Fig. 9a) is slight, and the structure looks almost like the flow shown in Fig. 4a. The front (i.e., region of increased density gradient at the bottom) consists almost entirely of buoyant inflow water. Stronger stratification (Fig. 9b) reduces the amount of buoyant inflow water that is carried offshore to the front, and the front is partially made up of ambient water. With the strongest stratification (Fig. 9c), much of the buoyant inflow water rides above the ambient water. The foot of the front consists almost entirely of ambient water, while the surface expression of the front is mostly buoyant inflow water. Only one or two frontal isopycnals shown extend from surface to bottom. Despite these qualitative differences in the density fields, the alongshelf velocity structures are remarkably similar for all three examples. The main differences are that, with stronger stratification, the alongshelf jet is located closer to the coast, consistent with (15), and it carries a larger amount of denser ambient water. It should also be noted that the near-bottom density structure seaward of the front (e.g., between 35 km $< y <$ 60 km in Fig. 9c) shows evidence of bottom boundary layer growth and adjustment of the velocity field much like the barotropic inflows considered theoretically by Chapman and Lentz (1997) and modeled numerically by Chapman (2000). The alongshelf velocity is small at the bottom, both shoreward and seaward of the front, with a slight reversal at the base of the front.

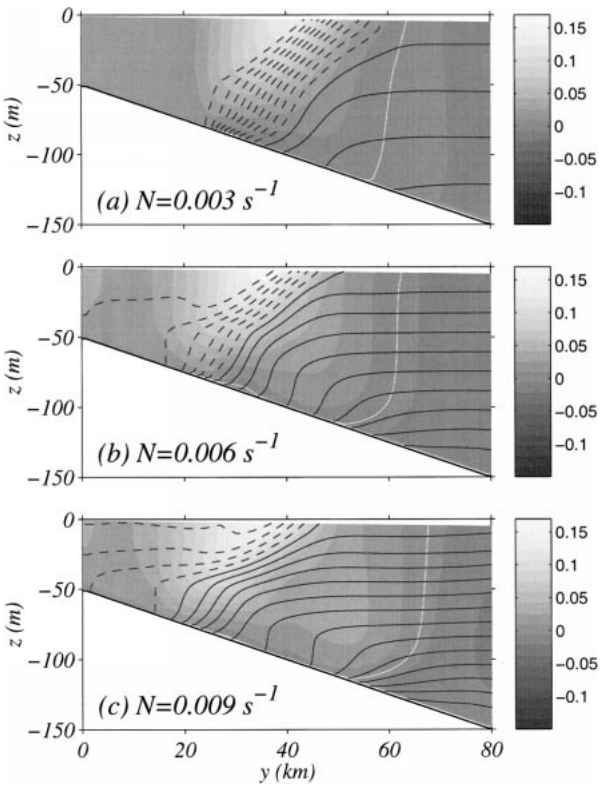

FIG. 9. Vertical sections of alongshelf velocity and density anomaly at $x = 120$ km after $t = 100$ days for a buoyant inflow with three different ambient stratifications. Shading shows u (m s^{-1}) with scale at right. White contours mark zero velocity. Other parameters are $\epsilon = 3 \times 10^{-4}$, $T_0 = 0.1336 \times 10^6$ m^3 s^{-1}, $h_0 = 100$ m, $y_0 = 20$ km, $f = 10^{-4}$ s^{-1}, $r = 5 \times 10^{-4}$ m s^{-1}. Density anomaly contours are (a) -0.28 to 0.11 by 0.03 kg m^{-3}, (b) -0.28 to 0.47 by 0.05 kg m^{-3}, (c) -0.28 to 1.08 by 0.08 kg m^{-3}. Dashed contours are buoyant inflow water. Solid contours are ambient water.

Figures 10 and 11 show selected views of the density anomalies and velocities for the medium stratification case ($N = 0.006$ s^{-1}, Fig. 9b), to be compared with the case of $N = 0$ shown in Figs. 3 and 4. There are two primary differences in the surface and bottom density

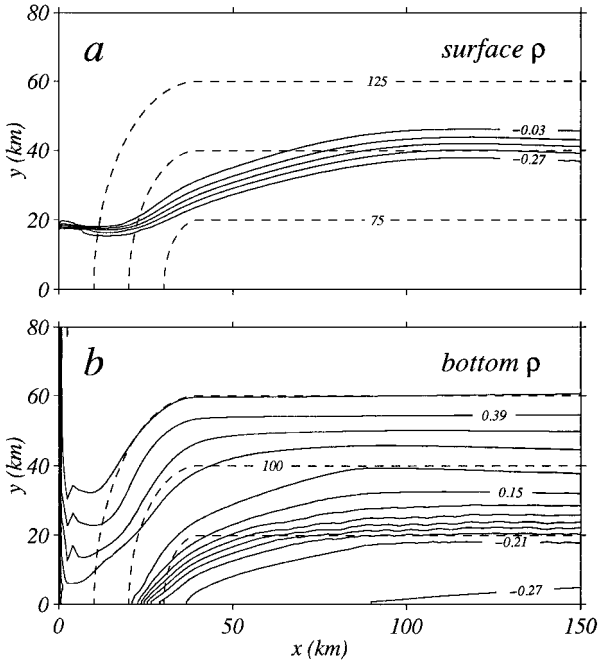

FIG. 10. Plan views of (a) surface and (b) bottom density anomalies after $t = 100$ days of a buoyant inflow with ambient stratification of $N = 6 \times 10^{-3}$ s^{-1}. Parameters are $\epsilon = 3 \times 10^{-4}$, $T_0 = 0.1336 \times 10^6$ m^3 s^{-1}, $h_0 = 100$ m, $y_0 = 20$ km, $f = 10^{-4}$ s^{-1}, $r = 5 \times 10^{-4}$ m s^{-1}. Contour interval is 0.06 kg m^{-3}. Dashed curves are selected isobaths. Only part of the model domain is shown; $L_x = 250$ km, $L_y = 120$ km.

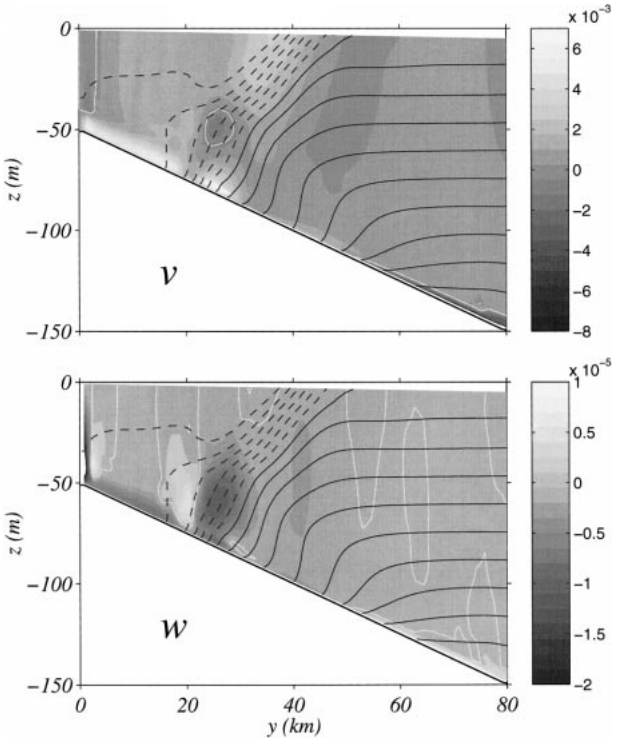

FIG. 11. Vertical sections of velocity and density anomaly for the calculation shown in Fig. 10 averaged over 112 km $< x <$ 122 km. Velocity values (m s^{-1}) are given by the shading bar at right. White contours mark zero velocities. Density anomaly contours are -0.28 to 0.47 by 0.05 kg m^{-3}. Dashed contours are buoyant inflow water. Solid contours are ambient water. Only part of the model domain is shown; $L_y = 120$ km.

anomalies (Fig. 10). First, ambient stratification has eliminated the surface bulge, so the surface density anomaly has reached a steady state. Second, the density anomaly at the bottom varies across the entire slope because of the ambient stratification, but the isopycnals are clearly bunched to form a front just seaward of the 75-m isobath ($-0.21 < \rho < 0.09$ kg m^{-3}). The cross-shelf and vertical velocities (Fig. 11) are qualitatively similar to those for the $N = 0$ case (Fig. 4); that is, there is a convergence of v in the bottom boundary layer near the shoreward side of the front, with a corresponding upward flow out of the boundary layer. The basic frontal trapping mechanism seems to be unchanged by ambient stratification.

Numerous calculations have been made with different ambient stratifications and various inflow properties to test (15). For each calculation, the frontal trapping depth is estimated in the downstream region, where the bottom isopycnals are parallel to the isobaths, by the depth at which the cross-shelf density gradient (ρ_y) at the bottom is maximum. These depths are then scaled to obtain $\hat{h}_*$ using the inflow transport T_0. The results are listed in Table 1 and plotted against γ in Fig. 12a, with the run number inside the symbol. The solid curve is the solution to (15). Circles represent calculations without ambient stratification reported in section 3 ($N = 0$, so $\gamma = 0$). Squares are cases with N ranging from 3 to 9 ($\times 10^{-3}$ s^{-1}) while holding all other parameters the same as the case shown in Figs. 9b, 10, and 11. Diamonds are cases with different inflow density anomalies but keeping $h_0 = 100$ m. Upward triangles are cases with increased inflow transport such that $h_0 = 150$ m. Downward triangles are cases with topography that includes a shelf break, discussed in section 5.

There is a clear tendency for increased stratification to reduce the trapping depth, that is, move the front closer to the coast. For small γ, the reduction is consistent with the analytical estimate (15). As γ increases, the trapping depth generally decreases more slowly than (15), indicating a breakdown of the conceptual model (i.e., assumptions) that led to (15). In these cases, the behavior is not as simple as has been assumed. For example, Fig. 13 shows results for the largest γ considered (run 12 in Table 1). As the inflow first encounters the topography (Fig. 13a), the buoyant water is confined to the upper 50 m of the water column, entirely above the ambient water with no contact at the bottom. The alongshelf velocity is nonzero throughout the water column over a wide region, so the flow adjusts much like a barotropic inflow. A front is formed from the ambient stratification, and the buoyant inflow remains as a surface-trapped feature through the length of the channel

TABLE 1. Parameters for calculations with ambient stratification. The frontal trapping isobath h_n and the alongshelf transport within the front T_s are estimated from the numerical results. In all cases, $f = 10^{-4}$ s^{-1} and $r = 5 \times 10^{-4}$ m s^{-1}. Downstream topography is a uniform bottom slope of 1.25×10^{-3} for runs 1–13. Runs 14–18 have shelf bottom slope of 1.25×10^{-3} with a shelf break at depth h_{sb}. Run 19 is identical to run 17 except that the shelf bottom slope is 0.001 so that the shelf break is located farther offshore.

Run	h_0 (m)	ϵ ($\times 10^{-4}$)	T_0 ($\times 10^6$ m^3 s^{-1})	N ($\times 10^{-3}$ s^{-1})	h_{sb} (m)	h_n (m)	T_s ($\times 10^6$ m^3 s^{-1})
1	100	3	0.1336	3		84	0.139
2	100	3	0.1336	4		81	0.146
3	100	3	0.1336	5		80	0.155
4	100	3	0.1336	6		78	0.164
5	100	3	0.1336	7		77	0.173
6	100	3	0.1336	8		75	0.185
7	100	3	0.1336	9		75	0.197
8	100	5	0.2227	6		79	0.240
9	100	1.5	0.0668	4.2		86	0.091
10	150	3	0.3119	3		122	0.333
11	150	3	0.3119	6		109	0.386
12	150	3	0.3119	9		106	0.409
13	150	5	0.5191	6		110	0.544
14	100	3	0.1358	6	100	78	0.201
15	150	3	0.2930	6	100	108	0.291
16	150	3	0.2993	6	75	111	0.353
17	150	3	0.2921	6	90	112	0.312
18	150	3	0.2917	9	90	114	0.528
19	150	3	0.2954	6	90	106	0.396

(Fig. 13b). The net result is that the front is located in deeper water than predicted by (15).

The largest source of error in obtaining (15) comes from equating frontal transport to inflow transport ($T_s = T_0$). The problem is that the frontal transport is augmented by the addition of ambient stratified waters, producing transports that can be considerably larger than the inflow transport (T_s in Table 1). The enhancement in frontal transport generally increases with increased stratification. If the true frontal transport is used to scale the trapping depth [i.e., scale h_* by $(2T_s f/\epsilon g)^{1/2}$], then the agreement with (15) is greatly improved (Fig. 12b). This is equivalent to a direct test of (14), indicating that the other assumptions are reasonable. The drawback to using T_s in (15) is that it is not known a priori, so the trapping depth cannot be predicted prior to each numerical calculation. For this reason, (15) with T_0 is preferred for estimating h_*, with the understanding that the true frontal trapping depth may be greater than h_*, but probably less than h_b. In this sense, (15) places bounds on the expected location of the trapped front.

5. Shelfbreak topography

The studies of Gawarkiewicz and Chapman (1992) and Chapman and Lentz (1997) both show that a sudden change in bottom slope (e.g., a shelf break) can significantly alter the behavior of a barotropic flow into a stratified ocean. As the flow moves beyond the shelf break, it encounters an increased density gradient along the bottom that causes a strong convergence in the bottom boundary layer and subsequent separation from the bottom. The flow is essentially trapped on the shelf and cannot penetrate far seaward of the shelf break. Whether or not a shelf break has a similar influence on the present frontal trapping mechanism was not considered in the two previous sections.

It might be expected that a shelf break would not strongly influence the case of $N = 0$ because there is no ambient stratification to produce the increased density gradient over the steeper slope. In fact, a shelf break has no noticeable impact on this case. Several calculations were made with shelfbreak topography, and the front is always trapped near h_b. An example, although not pointed out in section 3, is shown in Fig. 6. The shelf break is located at 75 m, and the front is trapped at about 145 m. (The shelfbreak is not obvious in Fig. 6. However, the distance between the coast, with $h_c = 50$ m, and the 100-m isobath is greater than the distance between the other isobaths, indicating a gentler slope near the coast.)

Greater influence of a shelf break might be expected in cases with ambient stratification. Several calculations were made to test this idea (Table 1), and again the shelf break has little impact, regardless of its location relative to the frontal trapping depth (Fig. 12). Runs 17–19 are an attempt to find even a secondary effect by locating the shelf break slightly shallower than the trapping isobath. This way, the increased density gradients along the bottom over the steeper slope might at least keep the foot of the front on the shelf. However, the shelf break has virtually no effect in each case. Figure 14 compares two calculations (runs 11 and 17) that are identical except for the presence of a shelf break (at 90 m). In both cases, $h_* = 105$ m and the front is located slightly deeper with the shelf break. The basic frontal structure is only slightly different. With the shelf break, the maximum surface velocity is slightly closer to the coast and the maximum cross-shelf density gra-

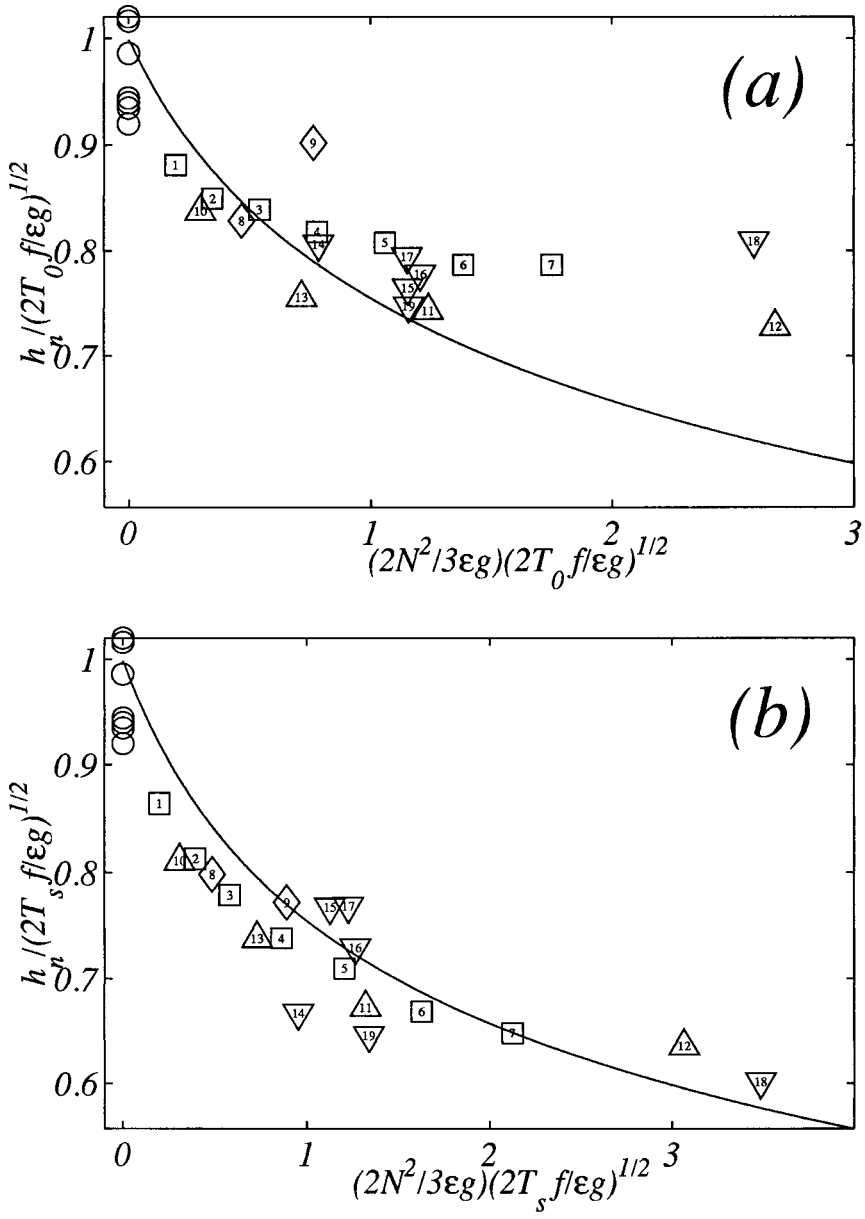

FIG. 12. Scaled trapping isobath $\hat{h}_*$ in (15) vs γ estimated from calculations with ambient stratification using (a) the buoyant inflow transport T_0 or (b) the numerically calculated frontal transport T_s to scale h_*. Numbers within symbols correspond to run numbers in Table 1. Circles are for unstratified ambient fluid (Fig. 7); squares are runs with $h_0 = 100$ m and N changing; upward triangles are runs with $h_0 = 150$ m; downward triangles are runs with shelf breaks. The solid curve is the solution to (15).

dient at the bottom is about twice as large, but these changes are minor. Clearly, the shelf break has not caused much change in frontal trapping.

6. Discussion

The results obtained here support the conclusion of previous studies that buoyancy advection in the bottom boundary layer profoundly affects the adjustment and evolution of stratified flows over sloping topography. In particular, the basic frontal trapping mechanism proposed by Chapman and Lentz (1994) operates both in deeper water than was previously tested, and in the presence of ambient stratification. In several ways, these results support the notion that the frontal trapping mechanism may play a role in shelfbreak front dynamics:

1) The abrupt bottom topography used here provides a

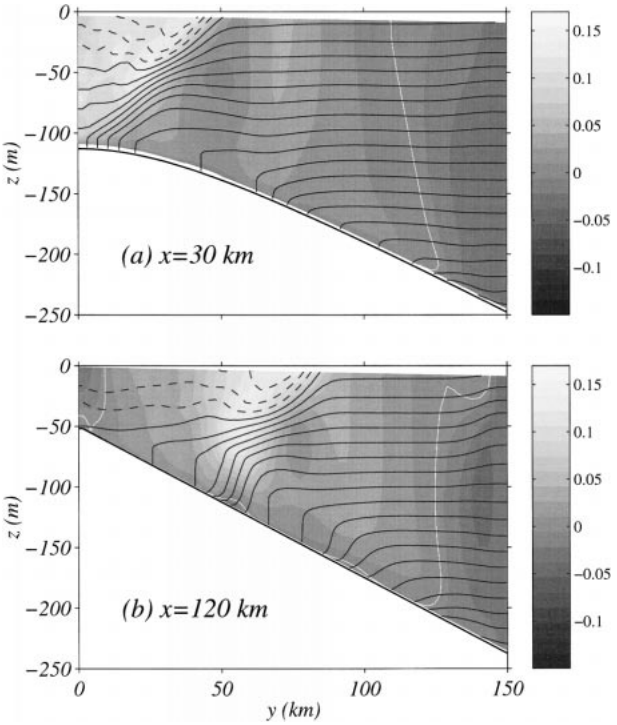

FIG. 13. Vertical sections of alongshelf velocity and density anomaly at (a) $x = 30$ km and (b) $x = 120$ km after $t = 100$ days for a buoyant inflow with ambient stratification of $N = 9 \times 10^{-3}$ s^{-1}. Shading shows u (m s^{-1}) with scale at right. White contours mark zero velocity. Other parameters are $\epsilon = 3 \times 10^{-4}$, $T_0 = 0.3119 \times 10^6$ m^3 s^{-1}, $h_0 = 150$ m, $y_0 = 30$ km, $f = 10^{-4}$ s^{-1}, $r = 5 \times 10^{-4}$ m s^{-1}. Density anomaly contours are -0.28 to 1.82 by 0.1 kg m^{-3}. Dashed contours are buoyant inflow water. Solid contours are ambient water. Only part of the model domain is shown; $L_y = 200$ km.

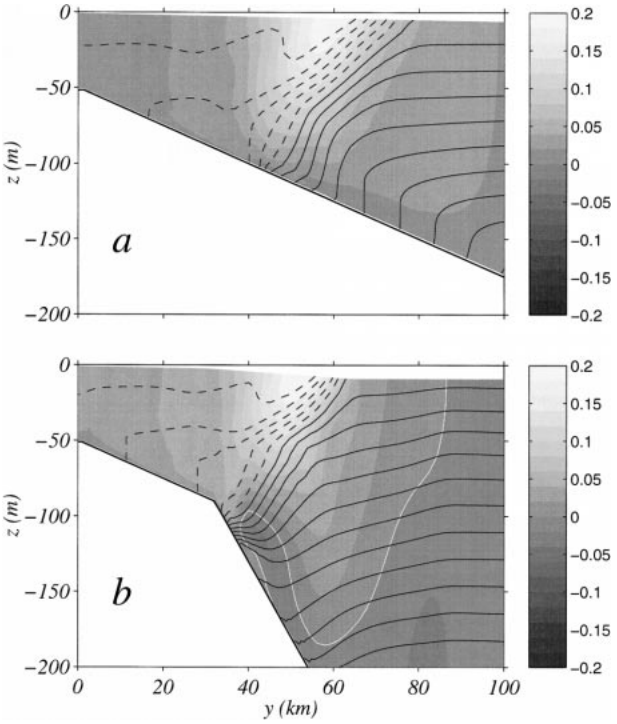

FIG. 14. Vertical sections of alongshelf velocity and density anomaly at $x = 120$ km after $t = 100$ days for a buoyant inflow with ambient stratification (a) without and (b) with a shelf break (at 90 m). Shading shows u (m s^{-1}) with scale at right. White contours mark zero velocity. Parameters are $N = 6 \times 10^{-3}$ s^{-1}, $\epsilon = 3 \times 10^{-4}$, $h_0 = 150$ m, $y_0 = 30$ km, $f = 10^{-4}$ s^{-1}, $r = 5 \times 10^{-4}$ m s^{-1}, and $T_0 = 0.3119 \times 10^6$ m^3 s^{-1} in (a) and $T_0 = 0.2921 \times 10^6$ m^3 s^{-1} in (b). Density anomaly contours are -0.28 to 0.74 by 0.06 kg m^{-3}. Dashed contours are buoyant inflow water. Solid contours are ambient water. Only part of each model domain is shown; (a) $L_y = 200$ km, (b) $L_y = 120$ km.

means of establishing a shelfbreak front within a relatively short alongshelf distance, in contrast to previous studies. This suggests that local bathymetry may account for the appearance of a sharp shelfbreak front both on the northern Labrador shelf south of Hudson Strait and along the southern flank of Georges Bank.

2) The density and velocity structures of some cases with ambient stratification (e.g., Figs. 9c and 13b) look qualitatively like some observed sections across the MAB shelfbreak front. For example, Pickart (2000) finds a similar density structure (cf. his Figs. 3 and 7) and reports a bottom boundary layer on both sides of the foot of the front. Only a few of the isopycnals extend from surface to bottom, and the alongshelf velocity is bowl-shaped, extending seaward of the front. All of these features can be seen in Figs. 9c and 13b.
3) Equations (1) and (15) can be used to make rough estimates of the range of frontal trapping depths for both the MAB and the Labrador shelf as follows. In the MAB, estimates for the parameters in the Nantucket Shoals region can be made from Linder and Gawarkiewicz (1998); $\epsilon \approx 0.5 \times 10^{-3}$, $T_0 \approx 0.24 \times 10^6$ m^3 s^{-1}, and $N^2 \approx 1.5 \times 10^{-4}$ s^{-2}. These values produce $h_b = 99$ m and $h_* = 65$ m, suggesting that ambient stratification could significantly change the frontal trapping depth here. The shelf break is located at about 100 m, close to h_b, and the foot of the shelfbreak front is observed to move seasonally between about 85 and 105 m, consistent with the range given by h_b and h_*. On the Labrador shelf, from Lazier and Wright (1993), the relative density anomaly across the shelfbreak front is $\epsilon \approx 0.7 \times 10^{-3}$, while the transport is $T_0 \approx 2.7 \times 10^6$ m^3 s^{-1}. The offshore stratification is quite weak at $N^2 \approx 4 \times 10^{-7}$ s^{-2}, so h_b and h_* are nearly equal, with $h_b = 280$ m and $h_* = 278$ m. This suggests that ambient stratification is not important in trapping the front along the Labrador shelf. Both estimates are somewhat deeper than the shelfbreak front that occurs at about 200 m, but perhaps not unreasonable considering the simplicity of the theory and the approximate estimates of the parameters.

An alternative explanation for the difference in the estimate of h_* on the Labrador shelf and the actual

position of the front is that the shelfbreak topography may significantly influence the frontal location. This possibility underscores perhaps the most intriguing model result: the *lack* of influence that the shelf break has on frontal trapping. With or without ambient stratification, the frontal trapping isobath in the numerical calculations is between h_* and h_b, regardless of the presence of the shelf break. This raises some basic questions. Is the shelf break dynamically important in determining the location of the shelfbreak front? If so, what are the dynamics? If not, are shelfbreak fronts located near the shelf break by coincidence? Linder and Gawarkiewicz (1998) show that the shelfbreak front remains near the shelfbreak through much of the MAB, despite southward shoaling of the shelfbreak. From the present results, this implies changes in the transport, density difference across the front and/or background stratification that continually adjust the trapping depth to the shelf break depth, the dynamics of which are unclear. Furthermore, such changes are not obvious from the observations. How does the front adjust to changes in the transport? Is transport lost from the front when it enters a region with a shallower shelf break? If so, how? What determines and limits the transport? Clearly the present study does not provide answers to these questions.

An unexpected effect of ambient stratification is its tendency to stabilize the upper portion of the front so that the surface bulge no longer develops (Fig. 10). The front can also be stabilized by imposing a weak inflow of ambient water through the upstream boundary at $x = 0$. For example, the calculation shown in Fig. 6 was repeated with a 0.025 m s^{-1} velocity added at the inflow boundary across the entire channel (at each y). Plan views of the surface and bottom density anomalies are shown in Fig. 15. The foot of the front is still trapped just shoreward of the 150-m isobath, but the surface expression of the front contains no bulge and no small-scale features like those in Fig. 6. This is consistent with the modeling study of Fong (1998), who considered a surface-trapped buoyant plume and found that the surface bulge could spread a finite distance offshore before eventually being swept downstream by the background inflow of ambient water. These stabilizing effects suggest that frontal instabilities are less likely to be the source of small-scale variations and eddies in shelfbreak fronts in cases where the ambient stratification and/or ambient currents are strong.

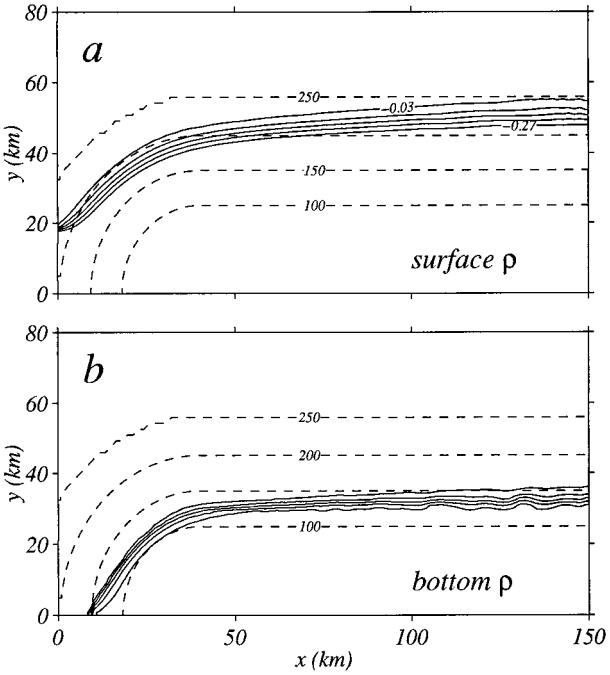

FIG. 15. Plan views of (a) surface and (b) bottom density anomalies after $t = 100$ days of a buoyant inflow into a homogeneous fluid with a background inflow of 0.025 m s^{-1} at the upstream boundary ($x = 0$). Otherwise, parameters are identical to Fig. 6: $\epsilon = 3 \times 10^{-4}$, $T_0 = 0.3052 \times 10^6$ m^3 s^{-1}, $h_0 = 150$ m, $y_0 = 20$ km, $f = 10^{-4}$ s^{-1}, $r = 5 \times 10^{-4}$ m s^{-1}. Contour interval is 0.06 kg m^{-3}. Dashed curves are selected isobaths.

7. Summary

The bottom boundary layer exerts a powerful control over buoyant coastal currents that contact the bottom; demonstrated here by modeling a buoyant current traveling along a vertical wall as it encounters bottom topography typical of a continental shelf. A surface-to-bottom front forms, and in the presence of bottom friction, the bottom boundary layer moves the front to a particular isobath where the front is trapped. The frontal trapping isobath for a buoyant inflow into a homogeneous fluid can be accurately estimated using (1). Ambient stratification keeps the front in shallower water, and (15) provides an estimate of the new trapping isobath. The agreement with the numerical calculations is not as good because the frontal transport may be increased by the addition of ambient stratified waters. Nevertheless, (1) and (15) provide bounds on the location of the trapped front. Furthermore, (15) provides a dynamical link between the adjustment of a buoyant inflow into a homogeneous fluid and a barotropic inflow into a stratified fluid.

The results support the notion that the frontal trapping mechanism may play a role in establishing a shelfbreak front. For instance, the mechanism operates in depths typical of shelf breaks, and the front can easily reach those depths in places where a large-scale buoyant current suddenly encounters shelf topography. Some model density and velocity fields look qualitatively like observed fields, and theoretical estimates of frontal location, based on (1) and (15), are in reasonable agreement with observed fronts in the MAB and on the Labrador shelf.

Several other features are worth noting. The frontal trapping mechanism is remarkably robust, in fact so robust that the presence of a shelf break has little effect

on the final location of the front. This raises questions about both the dynamical role of shelfbreak topography in frontal behavior and the applicability of the model to real shelfbreak fronts. These questions should be addressed in future studies. Bottom stress is necessary for frontal trapping, but the trapping location is relatively insensitive to the magnitude of the bottom friction coefficient. The near-surface part of the front is sometimes unstable, but it can be stabilized either by ambient stratification or by a weak background current in the direction of the buoyant inflow.

Acknowledgments. Many thanks to Steve Lentz who contributed to this work through his insightful questions and comments during numerous discussions. I also thank Bob Pickart, Rich Garvine, and an anonymous reviewer for their thoughtful comments and suggestions, which greatly improved the manuscript. I am grateful for the financial support provided by the Ocean Sciences Division of the National Science Foundation under Grant OCE-9809965.

REFERENCES

Abramowitz, M., and I. A. Stegun, 1968: *Handbook of Mathematical Functions.* Dover, 1046 pp.

Barth, J. A., D. Bogucki, S. D. Pierce, and P. M. Kosro, 1998: Secondary circulation associated with a shelfbreak front. *Geophys. Res. Lett.,* **25,** 2761–2764.

Chapman, D. C., 2000: A numerical study of the adjustment of a narrow stratified current over a sloping bottom. *J. Phys. Oceanogr.,* **30,** 2927–2940.

——, and R. C. Beardsley, 1989: On the origin of shelf water in the Middle Atlantic Bight. *J. Phys. Oceanogr.,* **19,** 384–391.

——, and S. J. Lentz, 1994: Trapping of a coastal density front by the bottom boundary layer. *J. Phys. Oceanogr.,* **24,** 1464–1479.

——, and ——, 1997: Adjustment of stratified flow over a sloping bottom. *J. Phys. Oceanogr.,* **27,** 340–356.

Condie, S. A., 1993: Formation and stability of shelf break fronts. *J. Geophys. Res.,* **98,** 12 405–12 416.

Fong, D. A., 1998: Dynamics of freshwater plumes: Observations and numerical modeling of the wind-forced response and alongshore freshwater transport. Ph.D. thesis, Woods Hole Oceanographic Institution, Massachusetts Institute of Technology, 172 pp.

Garvine, R. W., 1999: Penetration of buoyant coastal discharge onto the continental shelf: A numerical model experiment. *J. Phys. Oceanogr.,* **29,** 1892–1909.

Gawarkiewicz, G., and D. C. Chapman, 1992: The role of stratification in the formation and maintenance of shelfbreak fronts. *J. Phys. Oceanogr.,* **22,** 753–772.

Haidvogel, D., J. Wilkin, and R. Young, 1991: A semi-spectral primitive equation ocean circulation model using vertical sigma and orthogonal curvilinear horizontal coordinates. *J. Comput. Phys.,* **94,** 151–185.

Houghton, R. W., 1997: Lagrangian flow at the foot of a shelfbreak front using a dye tracer injected into the bottom boundary layer. *Geophys. Res. Lett.,* **24,** 2035–2038.

——, and M. Visbeck, 1998: Upwelling and convergence in the Middle Atlantic Bight shelfbreak front. *Geophys. Res. Lett.,* **25,** 2765–2768.

Khatiwala, S. P., R. G. Fairbanks, and R. W. Houghton, 1999: Freshwater sources to the coastal ocean off northeastern North America: Evidence from $H_2^{18}O/H_2^{16}O$. *J. Geophys. Res.,* **104,** 18 241–18 255.

Lazier, J. R. N., and D. G. Wright, 1993: Annual velocity variations in the Labrador Current. *J. Phys. Oceanogr.,* **23,** 659–678.

Linder, C. A., and G. Gawarkiewicz, 1998: A climatology of the shelfbreak front in the Middle Atlantic Bight. *J. Geophys. Res.,* **103,** 18 405–18 423.

Loder, J. W., B. Petrie, and G. Gawarkiewicz, 1998: The coastal ocean off northern North America: A large-scale view. *The Sea,* Vol. 11, *The Global Coastal Ocean. Regional Studies and Syntheses,* K. H. Brink and A. R. Robinson, Eds., Wiley and Sons, 105–133.

Narayanan, C., 1999: Offshore spreading of a buoyant coastal discharge. Ph.D. dissertation, University of Delaware, 267 pp. [Available from University of Delaware, Newark, DE 19716.]

Pickart, R. S., 2000: Bottom boundary layer structure and detachment in the shelfbreak jet of the Middle Atlantic Bight. *J. Phys. Oceanogr.,* **30,** 2668–2686.

——, D. J. Torres, T. K. McKee, M. J. Caruso, and J. E. Przystup, 1999: Diagnosing a meander of the shelf break current in the Middle Atlantic Bight. *J. Geophys. Res.,* **104,** 3121–3132.

Song, Y., and D. Haidvogel, 1994: A semi-implicit ocean circulation model using a generalized topography-following coordinate system. *J. Comput. Phys.,* **115,** 228–244.

Stommel, H., and A. Leetma, 1972: The circulation on the continental shelf. *Proc. Natl. Acad. Sci.,* **69,** 3380–3384.

Ullman, D. S., and P. C. Cornillon, 1999: Satellite-derived sea surface temperature fronts on the continental shelf off the northeast U.S. coast. *J. Geophys. Res.,* **104,** 23 459–23 478.

Willmott, A. J., and I. L. Collings, 1997: A steady state two-dimensional model for the maintenance of shelf break fronts. *Contin. Shelf Res.,* **17,** 1119–1139.

Wright, D. G., 1989: On the alongshelf evolution of an idealized density front. *J. Phys. Oceanogr.,* **19,** 532–541.

Yankovsky, A. E., and D. C. Chapman, 1997: A simple theory for the fate of buoyant coastal discharges. *J. Phys. Oceanogr.,* **27,** 1386–1401.